

Resolution in the ApoTome and the confocal laser scanning microscope: comparison

Arwed Weigel

Detlev Schild

André Zeug*

University of Göttingen

Department of Neurophysiology and Cellular Biophysics

Humboldtallee 23

37073 Göttingen, Germany

and

Deutsche Forschungsgemeinschaft-Research Center for the

Molecular Physiology of the Brain (FZT 103)

Göttingen, Germany

Abstract. The essential feature of the confocal laser scanning microscope (cLSM) is the generation of optical sections by the removal of out-of-focus light. About ten years ago, structured illumination microscopy (SIM) was introduced as an alternative method for obtaining optical sections from biological specimens. Here we compare the resolution of the ApoTome (commercial SIM by Zeiss) to that achieved by a cLSM (Zeiss LSM 510). If fluorescent beads are used as test objects, then the ApoTome will achieve a lower axial resolution than the cLSM. In contrast to that, its lateral resolution scores slightly better. If subresolution homogeneous fluorescent layers are used as test objects, then the ApoTome will achieve a higher axial resolution than the cLSM. The ApoTome's axial resolution is homogeneous over the field-of-view while that of the cLSM changes markedly. Finally, the anisotropy of the ApoTome's resolution was found to be negligible for standard applications while its capability to resolve fine structures within stained tissue slices is limited to one or two cell layers and thus worse than in the cLSM. © 2009 Society of Photo-Optical Instrumentation Engineers. [DOI: 10.1117/1.3083439]

Keywords: confocal microscopy; structured illumination microscopy; point spread function; resolution.

Paper 08297R received Aug. 25, 2008; revised manuscript received Dec. 22, 2008; accepted for publication Dec. 23, 2008; published online Feb. 25, 2009.

1 Introduction

In 1997, a new concept of microscopy appeared that allowed the rejection of out-of-focus light.¹ Differently from confocal optics, this method neither requires a laser as excitation source nor pixelwise scanning of the object. Instead, a single spatial frequency grating placed in the microscope's field stop plane is projected into the focal plane within the specimen so that the excitation intensity $I(x, y)$ is distributed as follows:

$$I(x, y) = I_0 + I_s \cos(2\pi \hat{v}x + \phi_0), \quad (1)$$

with I_0 and I_s being constants, \hat{v} the normalized grid frequency ($\hat{v} = M\lambda\nu_g/NA$), M the magnification between object plane and grid, λ the wavelength, ν_g the grid frequency, NA is the numerical aperture, and ϕ_0 is an arbitrary phase. Figure 1 shows the underlying principle. From the three images I_1 , I_2 , and I_3 , taken at grid positions ϕ_0 , $\phi_0 + (2/3)\pi$, and $\phi_0 + (4/3)\pi$, the optically sectioned image, I_s , is obtained by calculating

$$I_s = \frac{\sqrt{2}}{3} \sqrt{(I_1 - I_2)^2 + (I_2 - I_3)^2 + (I_3 - I_1)^2}, \quad (2)$$

and the conventional image can be recovered by

$$I_{\text{con}} = \frac{1}{3} \sum_{i=1}^3 I_i. \quad (3)$$

Variations and refinements of the basic realization include rotation of a grid in order to detect higher spatial frequencies based on Moiré fringes in two² and three dimensions,³ which, if combined with 4Pi-microscopy, yields up to 100 nm axial resolution,⁴ and focal intensity modulation through an interference pattern of two laser beams,⁵ laser illumination,⁶ and stripe-array illumination with light emitting diodes.⁷ In a setup with solid-state laser illumination, Cole et al.^{8,9} and Webb et al.¹⁰ used linear grid optical sectioning for fluorescence lifetime imaging microscopy measurements. An analysis of specific artifacts was performed by Schaefer et al.,¹¹ and their results were implemented into the Zeiss' AxioVision software. Karadaglić¹² and Karadaglić and Wilson¹³ refined the image formation theory in grid illumination, structured illumination microscopy (SIM), and discussed some sources of error. Lagerholm et al.¹⁴ gave an extended analysis of the proper utilization, potentials, and pitfalls of grid illumination. Chasles et al.¹⁵ quantitatively compared their custom SIM system to commercial SIM and confocal laser scanning microscope (cLSM) systems at fixed pinhole settings. Taken together, the properties of SIM have thus so far been characterized under various theoretical and practical aspects, but mainly in custom-tailored setups. A comparison of a commercially available SIM systems (thus far, Zeiss' ApoTome or

*Present address: Department of Cellular Neurophysiology, Hannover Medical School, Carl-Neuberg-Str. 1, 30625 Hanover, Germany. Address all correspondence to: André Zeug, Department of Cellular Neurophysiology, Hannover Medical School, Carl-Neuberg-Str. 1, 30625 Hanover, Germany. Tel: +49 511 532 4855; Fax +49 511 532 8302; E-mail: zeug.andre@mh-hannover.de

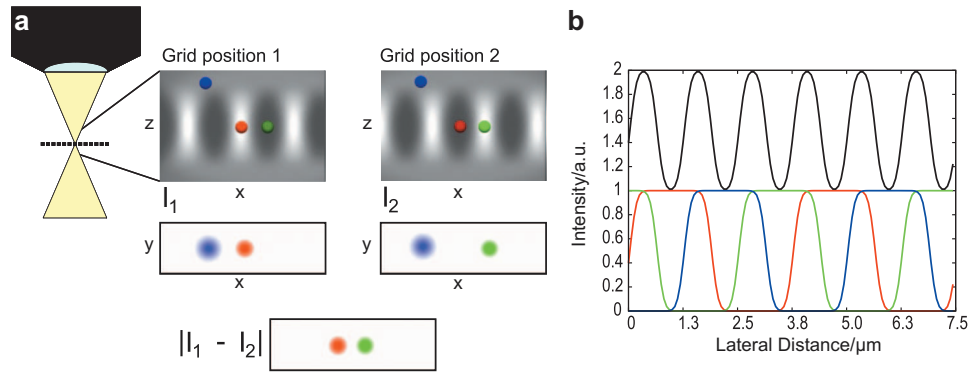


Fig. 1 (a) A simplified representation for the ApoTome principle demonstrates how optically sectioned images are obtained. In-focus structures are superposed by the grid pattern (red and green sphere) and therefore excited only in one or the other image. Thus, they are only visible in a subset of images. Out-of-focus structures appear blurred in both images (blue sphere). Sensitive depending on the proper grid positions, an alternate subtraction of the raw images readily yields the optically sectioned image. In the actual ApoTome algorithm, three images are taken (b) Red, green, and blue curve: grid pattern how they are imaged into the specimen for the calculation of one sectioned image. Black curve: intensity pattern that the specimen is exposed to during one sectioned image acquisition.

Qioptiq's OptiGrid) with a standard confocal laser scanning system is as yet lacking.

Here we therefore quantitatively analyze the imaging performance of the ApoTome under various aspects and compare it to that of a commercial confocal microscope (LSM 510).

2 Materials and Methods

2.1 Microscopes

For epifluorescence measurements, we used either an AxioObserver.Z1 or an Axiovert 200M (both Zeiss, Jena, Germany) equipped with a $40\times / 1.2\text{W}$ C-Apochromat or a $63\times / 1.4$ Oil Plan-Apochromat, and the Zeiss-filter sets 10, 49, 38 HE, 43, and 32. The AxioVision software (Zeiss, V. 4.6 or 4.4) was used to operate the microscope and readout of the charge-coupled device (CCD)-camera (AxioCam MRm, pixel size $6.45\ \mu\text{m} \times 6.45\ \mu\text{m}$, 1388×1040 pixels or AxioCam HR, $6.7\ \mu\text{m} \times 6.7\ \mu\text{m}$, 1300×1030 pixels). The illumination source was either a 120-W metal halide short-arc lamp (Exfo, Mississauga, Canada) or a xenon arc lamp (XBO 75).

For structured illumination measurements, the ApoTome-slider was introduced into the field-stop plane of one of the above microscopes. Thereby, one of two available rectangular-shaped gratings was inserted into the field-stop plane: either a grid with $\nu_{\text{VH}}=17.5$ lines/mm or a grid with $\nu_{\text{VL}}=35$ lines/mm. "VH" stands for the designated use with "high" magnification objectives, and "VL" stands for the designated use with "low" magnification objectives in an Axiovert microscope. If the $63\times / 1.4$ Oil Plan-Apochromat objective and $\lambda=500$ nm are used, the corresponding normalized grid frequencies are $\hat{\nu}_{\text{VH}}=0.15$ and $\hat{\nu}_{\text{VL}}=0.29$. Grid phase and focus calibration were performed prior to each experiment. For a z -stack, 60 sectioned images at 100-nm distance were taken. The acquired image stacks were exported as 16-bit TIFF images.

For cLSM measurements, the laser scanning unit LSM 510 (Zeiss) was attached to an Axiovert 100M that was equipped with the same objectives as above. The 488-nm laser line was used for excitation. Pinhole calibration was performed before every experiment. The pixel size was set to $71\ \text{nm} \times 71\ \text{nm}$

for the measurement of point-spread functions (PSFs), or to $285\ \text{nm} \times 285\ \text{nm}$ for measuring subresolution homogeneous fluorescent layers. Sixty images at 100 nm axial distance were taken. The cLSM setup was controlled by the LSM 510 software (V 3.2). Images were taken at 12 bit and exported as 12-bit TIFF files.

2.2 Test Objects: Fluorescent Beads, Layers, and Thin Dendrites

InSpeck Green microspheres (175 ± 5 nm) with a fluorescence coating ($\lambda_{\text{ex}}=505$ nm, $\lambda_{\text{em}}=515$ nm, Invitrogen, Karlsruhe, Germany) were used to measure PSFs. The experimentally determined PSFs are the result of the convolution of the test object (bead) with the imaging system transfer function and thus always affected by the test object's dimension. While the PSFs' axial extensions are nearly unaffected by this convolution, the lateral extensions are slightly higher than the actual microscope's resolution in the given high NA regime. The beads used are hence a compromise with respect to the available signal. The beads were dissolved in 70% ethanol, pipetted onto a cover slip, and allowed to dry. Mounting medium ($15\ \mu\text{L}$ Component E, Invitrogen, Karlsruhe, Germany) was then added and gently sealed by covering it with an object slide.

In order to measure how a subresolution homogeneous fluorescent layer in the object plane is imaged, we used reference layers fabricated as 100-nm thick fluoresceine/perylene diimid layers, which had a refractive index of $n_{\text{D}} \approx 1.59$.¹⁶

As test objects for anisotropic axial resolution, we prepared cell-cultures with small, straight-grown dendrites. The cell-culture preparation was done as described by Gennerich and Schild.¹⁷ Measurements were carried out within five to ten days after plating. Prior to the experiments, the cultures were loaded for 15 min with $100\ \mu\text{M}$ calcein-acetoxymethyl ester (Invitrogen, $\lambda_{\text{cm}}=514$ nm at pH 7.8), which was dissolved in dimethylsulfoxide (DMSO) and Pluronic F-127 (Invitrogen). The final concentrations of DMSO and Pluronic F-127 did not exceed 0.5 and 0.1%, respectively.

2.3 Tissue Preparation

Larvae of *Xenopus laevis* (stage 54 and older)¹⁸ were chilled in a mixture of ice and water and decapitated as approved by the Göttingen University Committee for Ethics in Animal Experimentation. A block of tissue containing the anterior two-thirds of the olfactory bulb was extirpated and glued onto the stage of a vibroslicer (VT 1000S; Leica, Bensheim, Germany). A tissue slice of $\approx 300\text{-}\mu\text{m}$ thickness containing the glomerular layer was cut out and transferred to a patch clamp setup. The whole cell configuration was established, and the cell was loaded ≈ 1 min with Alexa Fluor 488 biocytin (Invitrogen). After another 20 min, the tissue block was turned upside down and imaged under the ApoTome and the cLSM by using an axial stepwidth of $1.5\ \mu\text{m}$ (overview) or $0.45\ \mu\text{m}$ (selected positions).

Multicolour tissue visualization was prepared in four subsequent steps. (i) For tracing olfactory nerve fibers, some crystals of Alexa Fluor 488 biocytin were placed into the cut olfactory nerve of chilled tadpoles and the lesion was closed with cyanoacrylic glue (Roti-Coll 1, Roth, Karlsruhe, Germany). The tadpole was decapitated 3 h later, as described above, and a block of tissue containing the olfactory nerves and the anterior two-thirds of the brain were cut out and kept in a bath solution. (ii) A solution containing Alexa Fluor 546 biocytin was injected into the olfactory tract, and the tissue was incubated for another 2 h. Then, the tissue block was fixed in 4% formaldehyde in 0.1 M phosphate buffered saline (PBS) for ≈ 2 h, washed in PBS (3×10 min), embedded in agarose, glued onto the stage of a vibroslicer (VT 1000S; Leica, Bensheim, Germany), and cut into slices of $70\text{-}\mu\text{m}$ thickness. (iii) The slices were incubated in PBS containing 1% bovine serum albumin (BSA) for 30 min at room temperature. Then, they were incubated overnight in Alexa Fluor 647 Phalloidin (Invitrogen) ($5\ \mu\text{L}$ from methanol stock solution) in $200\ \mu\text{L}$ of PBS with 1% BSA. (iv) For further staining with 4',6-diamidino-2-phenylindole [(DAPI) Invitrogen], the slices were washed 3×10 min in PBS and incubated for 15 min in a mixture of 1 mL of PBS and $2\ \mu\text{L}$ of DAPI stock solution. After washing in PBS 5×10 min, they were mounted on object slides with DAKO Cytomation (Hamburg, Germany) Fluorescence Mounting Medium S3023.

2.4 Solutions

2.4.1 Bath solution

The composition of the bath solution was (in mM): NaCl, 98; KCl, 2; CaCl_2 , 1; MgCl_2 , 2; glucose, 5; sodium pyruvate, 5; and 4-(2-hydroxyethyl)-1-piperazineethanesulfonic acid (HEPES), 10. The pH was adjusted to 7.8 because this is the physiological pH in this poikilothermal species.¹⁹

2.4.2 Pipette solution

The composition of the intracellular solution was (in mM): NaCl, 2; KCl, 11; MgSO_4 , 2; K-gluconate, 80; HEPES, 10; ethylene glycol tetraacetic acid, 0.2; Na_2ATP , 2; and Na_2GTP , 0.2. The osmolarity was adjusted to 190 mOsm, and the pH to 7.8.

2.4.3 PBS

The composition of the 0.1 M PBS solution was (in mM): NaCl, 27.4; KCl, 0.54; Na_2HPO_4 , 1.6; and KH_2PO_4 , 0.28. The pH was adjusted to 7.4.

All chemicals required for the solutions above were purchased at Sigma (Deisenhofen, Germany).

2.5 Analysis

Data analysis was done by using programs written in Matlab. In order to determine the PSFs, single-bead images were cropped. The lateral resolution was obtained from a 2-D-Gaussian fit to the center-of-gravity (COG) plane. The axial resolution was obtained from a 1-D skewed Gaussian fit to the column containing the COG. χ_R^2 did not improve if the theoretically more precise descriptions for the axial and lateral PSF behavior are used.²⁰ The cropped PSFs were then aligned to the COG with subpixel precision and summed up.

Our Matlab Sectioned Image Property chart (SIPchart) analysis¹⁶ allowed freely selectable binning filters and free choice of a number of fit functions. Thus, ApoTome data were fitted by using a skewed Gaussian, where the z coordinate was assumed to follow $z' = z \exp(-sz)$, with s being the skew factor, and $I = I_0 \exp(-z'^2/2\sigma^2)$. cLSM data were fitted by using a skewed Lorentzian with $I = I_0[\sigma^2/(\sigma^2 + 4z'^2)]$.

3 Results and Discussion

3.1 Lateral Resolution

We measured the PSFs of fluorescent beads by using a $63 \times / 1.4$ Oil Plan-Apochromat objective (Zeiss) in order to compare the resolving power of the ApoTome with epifluorescence and confocal microscopes.²¹ The radial and the axial projections of the resulting PSFs are shown in Fig. 2 for epifluorescence [Fig. 2(a)], for the ApoTome with the VH grid or VL grid [Figs. 2(b) and 2(c)], and for the cLSM [Fig. 2(d)]. There is no significant difference between the ApoTome and the standard epifluorescence microscope with regard to lateral resolution, whereas the cLSM's PSF was slightly broader. Two noncommercial implementations of structured illumination^{2,22} are reported to have a lateral resolution higher than this. Note that SIM as realized in the ApoTome is not a linear-shift invariant system [cf. Eq. (2)]. Thus, it is not possible to describe the process of obtaining an ApoTome image in terms of the PSF for the general case. To this end, a set of fluorescent test samples containing all spatial frequencies in a defined manner would be required. Karadaglic and Wilson¹³ showed that in the case of defocus the features around the frequency ν are enhanced. This effect appears in the interaction between the object's zeroth spatial frequency and the frequencies close to ν . The PSF is still a useful measure of the resolution though less informative when imaging complex structures.

The resolution of the cLSM is determined by the size of the emission pinhole, and for maximally closed pinholes, theory predicts an improvement of $\sqrt{2}$ over epifluorescence,²³ where 95% of the in-focus light is rejected by the pinhole. A pinhole size of $d_p = 1$ Airy unit (A.U.) is often considered a good compromise between resolution and detected light intensity.²⁴ If, in this case, the backfocal plane (BFP) is illuminated homogeneously, then the lateral resolution of the

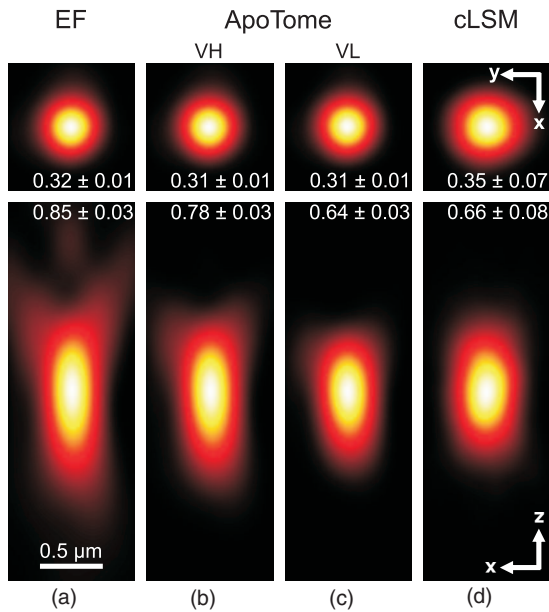


Fig. 2 (a–d) Lateral and axial PSFs obtained from 175 ± 5 nm green fluorescent beads embedded in component E. PSFs were produced by manually selecting ≥ 100 bead images for every imaging mode, aligning them with subpixel precision to their center of gravity, and calculating the mean. The axial resolutions in the cLSM determined with $d_p = 1$ A.U. and in the ApoTome determined with the VL grid are similar. VH, ApoTome low sectioning ($\hat{\nu}_{VH} = 0.15$); VL, ApoTome high sectioning ($\hat{\nu}_{VL} = 0.29$); EF, conventional epifluorescence. See text for further explanation.

cLSM should outperform epifluorescence by $\lambda_{cm}/\lambda_{ex}$. In our measurements, the cLSM's lateral resolution fell behind that of epifluorescence or the ApoTome: $d_{l,EF/VH/VL} \cdot 1.1 = d_{l,cLSM}$. This may be explained, first, by the Gaussian intensity profile in the BFP, which reduced the effective NA.²⁵ A second explanation is that the axial resolution is distributed spatially inhomogeneous (see below).

3.2 Axial Resolution

It is customary to determine a microscope's axial resolution with fluorescent beads. Fluorescently labelled biological ob-

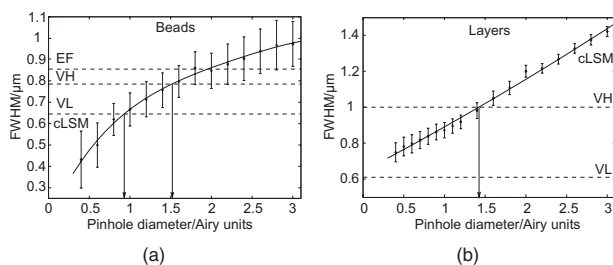


Fig. 3 Axial resolution as a function of the pinhole diameter determined by the use of fluorescent beads (a), and subresolution homogeneous fluorescent layers (b). If the pinhole is opened, then the axial resolution increases in a subproportional way in the case of using fluorescent beads. It increases almost linearly if fluorescent layers are used. The diameter of the pinhole d_p is given in A.U. as it appears back projected in the focal region. For comparison, the ApoTome resolution values are given as indicated. VH, ApoTome low sectioning ($\hat{\nu}_{VH} = 0.15$); VL, ApoTome high sectioning ($\hat{\nu}_{VL} = 0.29$).

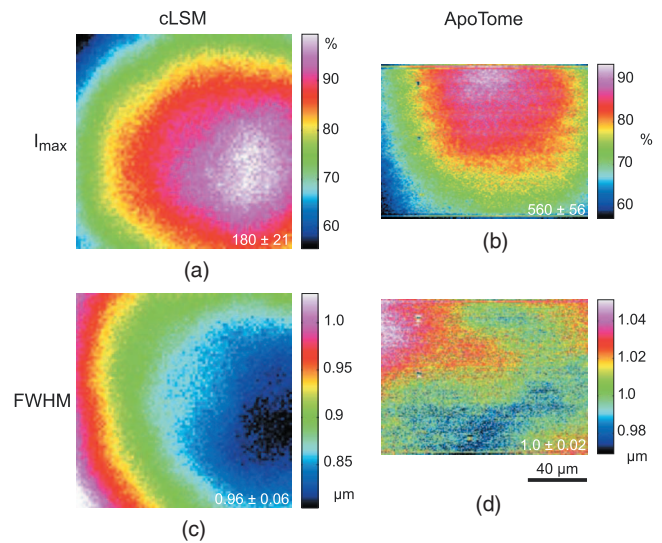


Fig. 4 (a–d) Extract of SIPcharts: a thin homogeneous fluorescent layer was recorded in a 3-D image stack, axial step size 100 nm, and subsequently processed to obtain SIPcharts, of which the extracts above directly compare illumination and resolution properties of the ApoTome (VH grid) and the cLSM system ($d_p = 1$ A.U.). The maximum intensity I_{max} has a circular-symmetric shape in both imaging modes, which is ascribed to chromatic and spherical aberration. Without the application of a spatial filter, there remain stripe artifacts induced by improper phase shifts of the grid, intensity fluctuations, and stage movements during acquisition and bleaching. The blots in the ApoTome images stem from a residue on the grid, underlining the importance of keeping it perfectly clean. Values (insets) refer to binned data sets mean \pm sd over the whole field of view (ApoTome: 8×2 binning mask to conserve the stripe pattern of the 1388×1040 pixels image: one period of the grid pattern is sampled by ≈ 23 pixels (VH grid) or ≈ 11.5 pixels (VL grid), leading to an artifact stripe pattern of $3 \times$ the grid pattern; cLSM: 6×6 binning mask for a 512×512 pixels image); objective: $63 \times / 1.4$ Oil Plan-Apochromat.

jects are however often rather densely, almost homogeneously stained, so that a fluorescent layer would seem a more adequate test object to determine axial resolution. Here we start by using beads as test objects, and will then use subresolution homogeneous fluorescent layers.

The axial resolution determined with beads differed markedly in the three microscopes analyzed. The full-width-at-half-maximum (FWHM) values of the axial Gaussian fits (Fig. 2, lower row) clearly show (i) that the ApoTome's axial resolution is better than that of the epifluorescence microscope, (ii) that the ApoTome's axial resolution depends on the grid used, and (iii) that the ApoTome's axial resolution with the VL grid is about the same as that of the cLSM (at a pinhole diameter of $d_p = 1$ A.U.). In conventional epifluorescence, the bead images show the characteristic butterfly-shaped side lobes as predicted by electromagnetic wave theory.²⁰ These are clearly reduced in the ApoTome. If the finer grid (VL) is used, then the ApoTome yields a 33% advantage over conventional epifluorescence and matches the cLSM's resolution.

Figure 3 shows the axial resolution (i) of the cLSM as a function of the pinhole diameter, (ii) of the ApoTome equipped with the VH grid ($\hat{\nu}_{VH} = 0.15$), (iii) of the ApoTome equipped with the VL grid ($\hat{\nu}_{VH} = 0.29$), and (iv) of epifluo-

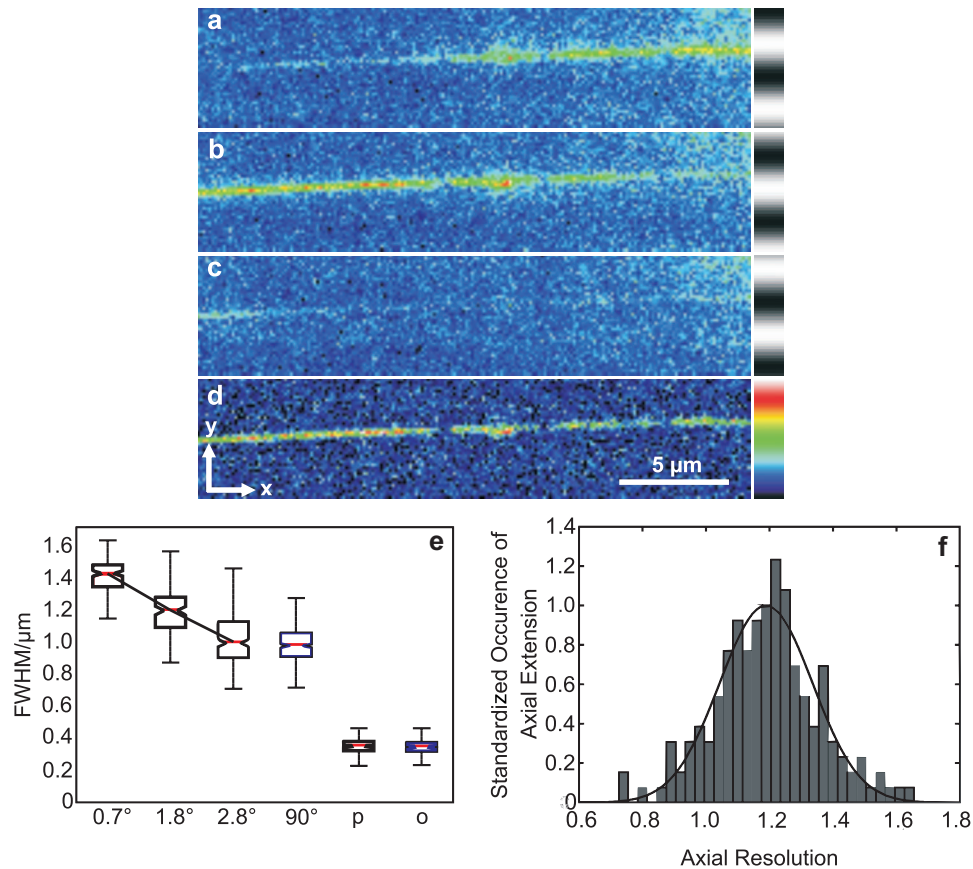


Fig. 5 Anisotropic resolution in the ApoTome. Straight-grown, smooth, fluorescence-labelled dendrites from cell cultures of olfactory bulb neurons of *Xenopus laevis* were recorded as image stacks at several angles to the grid pattern. In the example shown (a–d), the angle is 2.8 deg (a–c) raw images, right: illumination pattern giving the image to the left, and (d) processed images, right: color bar for (a–d). A 2-D Gaussian fit was applied to the corresponding image plane (either xz or yz plane) (e) An analysis of each dendrite reveals a rapidly increasing resolution with increasing angle to the grid. The lateral extension of the dendrites in the xy plane does not depend on the angle between the dendrite and the grid. It was $0.350 \pm 0.005 \mu\text{m}$ (mean \pm sd) in case the dendrite was parallel (p) to the grid, and $0.347 \pm 0.005 \mu\text{m}$ if it was orthogonal (o) to the grid (f) Normalized distribution of the axial extension of the dendrite tilted 1.8 deg obtained from ≥ 300 fits to the xz plane. The Gaussian distribution of the observable resolution supports the hypothesis that the dendrites' extensions are below the resolution limit.

rescence illumination determined with beads [Fig. 3(a)] and layers [Fig. 3(b)]. If the axial resolution was determined with beads, then the use of the ApoTome's VH grid corresponds to $d_p \approx 1.5$ A.U. in the cLSM, whereas the use of the VL grid corresponds to $d_p \approx 1$ A.U. Certainly, with increasingly smaller pinhole sizes, there is a marked increase in resolution (e.g., $0.43 \pm 0.14 \mu\text{m}$ at $d_p = 0.4$ A.U.). This outperforms the ApoTome's best bead resolution. It can also be seen from Fig. 3 a that for large pinhole sizes ($d_p \geq 2$ A.U.), the cLSM shows worse axial resolution than the epifluorescence microscope due to the Gaussian illumination of the BFP in the cLSM [i.e., due to the effect that the effective NA in the cLSM is lower than the nominal one, which is indicated on the objective barrel (here, 1.4)].

If the axial resolution is determined with subresolution homogeneous fluorescent layers, then the VL grid of the ApoTome will have about twice the resolution compared to the VH grid. This is expected from the twice-finer-grid structure and the corresponding cutoff frequency. Under these conditions, the ApoTome achieves a better resolution than the cLSM with a pinhole at minimum diameter [Fig. 3(b)]. For these comparisons, we took into account the bigger field of

view of the cLSM by cropping a field of view corresponding to the size of the ApoTome's field of view from the cLSM image. Because the axial resolution in the cLSM varied with the distance from the optical axis (see Section 3.3), the centerline of the crop stack was determined by the highest resolution.

3.3 Spatial Inhomogeneity of Axial Resolution

To investigate the possibility that the axial resolution was spatially inhomogeneously distributed, one can either measure bead PSFs at multiple distances from the optical axis (which is rather impractical) or use SIPcharts.¹⁶ These are generated from image stacks of a subresolution homogeneous fluorescent layer.

The SIPchart intensity distribution clearly showed radial symmetry both for the cLSM [Fig. 4(a)] and for the ApoTome [Fig. 4(b)]. Moreover, the axial resolution in the cLSM was highly correlated with the radial intensity distribution [Fig. 4(c)]. The symmetric shape can be ascribed to spherical and chromatic aberrations, while the off-axis resolution maximum can presumably be attributed to a slightly imperfect pinhole

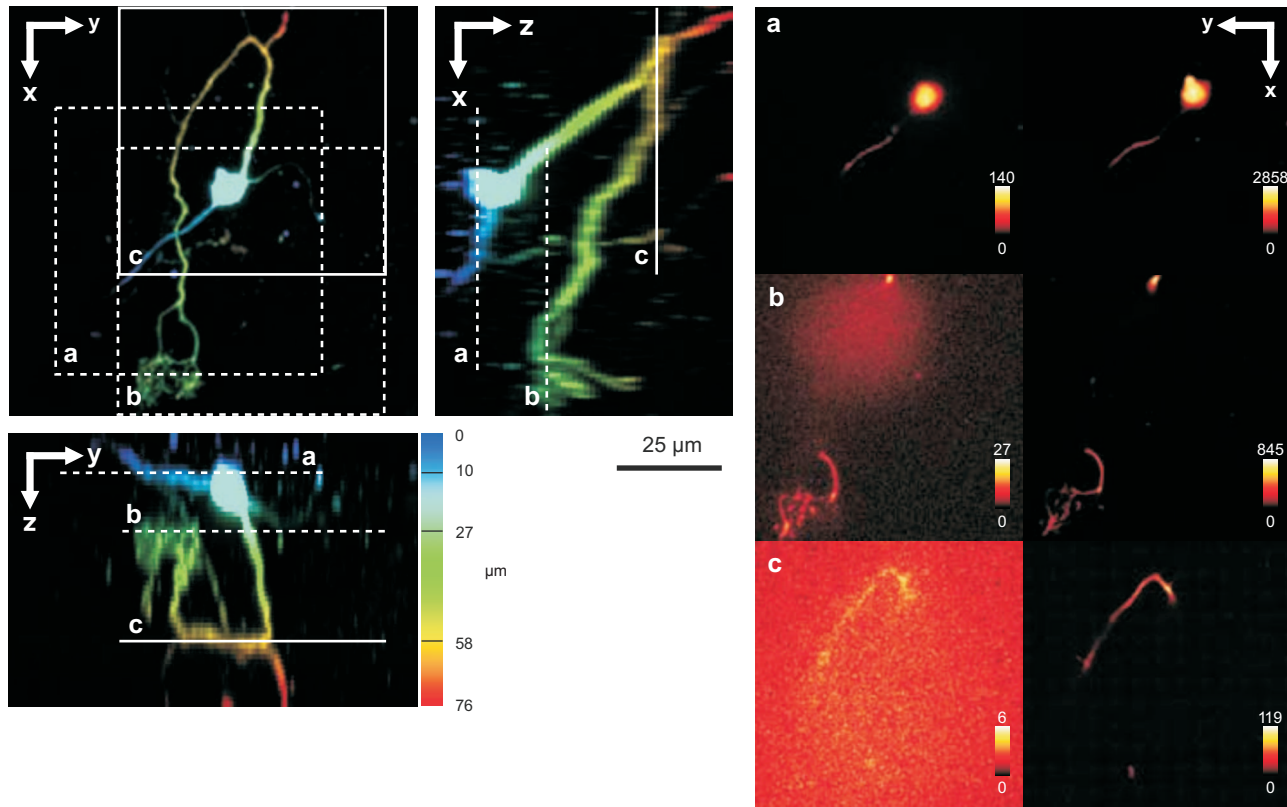


Fig. 6 A mitral cell in the olfactory bulb loaded with Alexa Fluor 488 biocytin through a patch pipette. Maximum projections in (a) xy , (b) xz , and (c) yz calculated from a stack of cLSM images. The color is used to code the z coordinate (see color bar). In addition, images were taken from the same tissue volume with the ApoTome. (d) Comparison of ApoTome optical sections (left column) and cLSM sections (right column) taken at the planes a, b, and c as indicated in the maximum projections ($a=10\ \mu\text{m}$, $b=27\ \mu\text{m}$, $c=58\ \mu\text{m}$). At $z=27\ \mu\text{m}$, the ApoTome image is markedly corrupted from noise caused by the brightly stained soma above the focal plane. At greater depths, in the ApoTome the noise becomes dominant with increasingly low contrast (see scale bar) while the cLSM still yields high contrast images with a contrast nearly as high as in the ApoTome at $z=10\ \mu\text{m}$.

adjustment. Remarkably, there is a difference of $\approx 250\ \text{nm}$ (22% or $\lambda/2$) between the best resolved regions at the intensity maximum and the worst resolved regions [see Fig. 4(c)]. Thus, the radial symmetry of and the change in axial resolution indicate that the specific position in the field of view in a cLSM image determines at which precision a subcellular structure can be resolved. Contrary to the cLSM, the ApoTome's axial resolution appears to be quite homogeneous, the deviations being $\leq \lambda/10$.

Interestingly, another feature of the ApoTome can be derived from the SIPcharts shown in Figs. 4(b) and 4(d); both reveal an artifact stripe pattern, which may result from stage vibrations leading to nonstationary imaging of the grid into the sample, imprecise phase shifts of the grid, bleaching of the grid pattern into the sample, or intensity fluctuations of the illumination arc source. The AxioVision software includes a digital filter that removes certain spatial frequencies in the Fourier domain. We found that the so-called weak filter was the best to remove the stripe artifacts under most imaging conditions. But the SIPcharts produced with the "weak filter" setting led to a substantial loss in axial resolution, namely, $1.2 \pm 0.03\ \mu\text{m}$ versus $1.0 \pm 0.02\ \mu\text{m}$ (VH) and $0.69 \pm 0.05\ \mu\text{m}$ versus $0.61 \pm 0.05\ \mu\text{m}$ (VL). Certainly, it can be expected that spatial low-pass filtering reduces spatial resolution. Because the AxioVision filtering algorithms are

not documented, the user applying a spatial filter to remove the stripe artifacts must find out, empirically, the impact of the filter used on axial resolution.

3.4 Anisotropy of Resolution

The ApoTome's grid-shaped illumination being 1-D modulated suggested that its axial resolution might be anisotropic. To test this, we measured the axial extensions of small and straight fluorescence-labeled neuronal dendrites in cell culture, taking the angle between dendrite and grid pattern as the parameter (Fig. 5). The lateral extensions of the dendrites were virtually independent of their orientation with respect to the grid [$350 \pm 5\ \text{nm}$ (parallel) and $347 \pm 5\ \text{nm}$ (orthogonal), mean \pm sd]. In contrast to that, the axial extension of dendrites oriented in a parallel way was significantly larger than that of dendrites oriented in an orthogonal way, with the angle dependency of the axial resolution being rather steep, assuming the value for orthogonal dendrites for less than $\alpha=3\ \text{deg}$ (Fig. 5).

3.5 Deep-Tissue Imaging

Because it is of practical relevance how well an optical sectioning technique works within stained biological tissue, we stained mitral cells of the olfactory bulb with Alexa Fluor 488

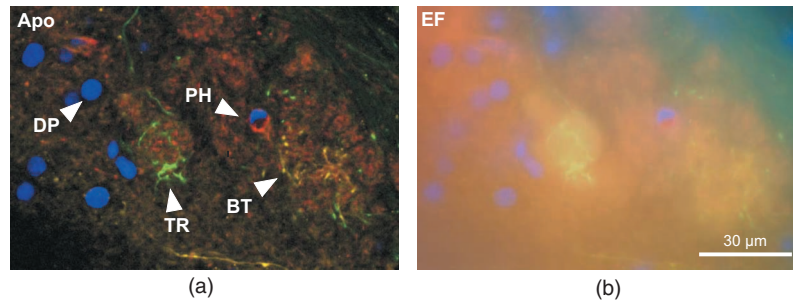


Fig. 7 A 70- μm thick section of the olfactory bulb of a *X. laevis* tadpole: blue: nuclei (DAPI), green: axons (Alexa Fluor 488 tracing), yellow: dendrites (Alexa Fluor 546 biocytin backtracing), red: actin-filaments (Alexa Fluor 647 phalloidin immunostaining). (a) ApoTome image and (b) conventional epifluorescence image. The sectioning makes it possible to clearly separate the four color channels. The axonal innervation of two glomeruli and the dendritic innervation of one of them can be seen. To a certain extent, the phalloidin staining is present in the whole tissue and especially in the two blood vessels included in the image, whereas the DAPI staining reveals that there are few cells in the glomerular layer. Erythrocytes show autofluorescence in the DAPI channel.

biocytin through a patch pipette and imaged the same cells by using the cLSM 510 and the ApoTome (Fig. 6). Morphological details close to the surface of the tissue can be resolved equally well in the ApoTome and the cLSM (plane a of Fig. 6), but in greater depths (planes b and c of Fig. 6) the ApoTome images show increased blur and noise. In plane b, for instance, the image plane cutting a dendrite is well below the cell's soma. The dendrite cut is clearly seen in both the ApoTome and the cLSM, but in addition, the ApoTome image shows a blurry spot, which is not seen in the cLSM image, reporting the noise originating from the soma above that plane; this is because the ApoTome, though taking into account out-of-focus light while calculating an optical section, does not remove the noise of out-of-focus light.²⁶ At imaging depths of several cell layers, the noise component becomes dominant in the ApoTome, preventing the acquisition of feature-rich images; at the same depth in the same preparation, the cLSM can still extract tiny structures (plane c of Fig. 6). This is of course due to out-of-focus photons being confocally suppressed in the cLSM. In the ApoTome in contrast, the grid pattern projected onto the focus plane is increasingly superimposed by scattered light at greater tissue depth. Moreover, its in-focus modulation is correspondingly attenuated with stronger staining; these effects are not taken into account by Eqs. (1)–(3).

3.6 Spectral Versatility

Figure 7 shows the ApoTome's spectral range of operation, which extends from near ultraviolet (UV) to near infrared. Commonly, cLSMs are not equipped with UV excitation so that the ApoTome may be preferred in cases where multicolor stainings are to be done. Figure 7 shows images of the olfactory bulb of a *X. laevis* tadpole stained with four different dyes, taken with a conventional epifluorescence microscope [Fig. 7(a)] or the ApoTome [Fig. 7(b)]. Clearly, the ApoTome removes most of the out-of-focus blur seen in epifluorescence mode.

4 Conclusion

4.1 Resolution

The ApoTome can achieve a better lateral resolution than the cLSM. The axial resolution of the ApoTome is in the same

range as the confocal one, depending on the particular conditions. If bead PSFs are measured close to the cover slip surface and under standard conditions ($d_p=1$ A.U.), then the axial resolution of the cLSM will be superior ($d_{z,\text{VH}}=0.78$ μm , $d_{z,\text{cLSM}}=0.66$ μm). If a subresolution fluorescent layer is measured, then the axial resolution of the ApoTome (with the VL grid) is superior ($d_{z,\text{VL}}=0.61$ μm , $d_{z,\text{cLSM}}=0.86$ μm at $d_p=1$ A.U. and $d_{z,\text{cLSM}}=0.75$ μm at $d_p=0.4$ A.U.).

4.2 Homogeneity of Resolution

Both cLSM and ApoTome show a radial distribution of excitation light intensity in the object plane. In the cLSM, the axial resolution varies markedly with radial symmetry, whereas the axial resolution in the ApoTome is rather constant, the deviations being in the order of $\lambda/10$.

4.3 Penetration Depth

The projection of both grid pattern or laser excitation onto the object plane within a tissue slice is affected by scattering in the tissue. Furthermore, the modulation amplitude of the grid pattern strongly depends on the integrated axial fluorescence intensity. In the cLSM, only the light coming directly from the focal volume is projected through the exit pinhole onto the photon detector. This way, out-of-focus light is mostly rejected. Because this spatial filtering effect is lacking in the ApoTome, images are increasingly deteriorated with increasing tissue depth, depending on the scattering within the tissue and staining intensity. Additionally, in the ApoTome, noise is counted as information. Because the ApoTome is a wide-field technique, the Poissonian noise contribution of any fluorescing probe in the beam path will be present in the optically sectioned image. The cLSM (or two-photon excitation microscopy) is thus preferred for imaging within slices or tissue blocks.

4.4 Acquisition Speed

Both systems, cLSM and ApoTome, are notoriously slow. In the ApoTome, the CCD readout rate, the number of color channels, and the necessity of taking three images for one are the major limiting factors, whereas in the cLSM, the image

acquisition rate can be increased by choosing a smaller field of view and a shorter pixel dwell time, both at a certain cost.

4.5 Bleaching

The ApoTome is prone to patterned bleaching. In observation mode, the manufacturer tries to avoid patterned bleaching by sinusoidally moving the grid. But once the acquisition has started in the three images equal-phase-shift approach, half of the specimen is illuminated two-third of the three-image acquisition time, whereas the other half is illuminated one-third of the total acquisition time. This creates patterned bleaching with three times the grid frequency.^{8,11} This artifact can be reduced at the cost of axial resolution.

Acknowledgments

We thank Stephan Junek for support in the microinjection experiment, and Eugen Kludt and Gudrun Federkeil for help with the four-color staining. We also thank J. M. Zwier (Swammerdam Institute for Life Sciences, Section of Molecular Cytology and Center of Advanced Microscopy, University of Amsterdam, The Netherlands) for generously providing us with the subresolution homogeneous fluorescent layer. This work was supported by the Deutsche Forschungsgemeinschaft through the DFG-Research Center Molecular Physiology of the Brain.

References

1. M. A. A. Neil, R. Juškaitis, and T. Wilson, "Method of obtaining optical sectioning by using structured light in a conventional microscope," *Opt. Lett.* **22**, 1905–1907 (1997).
2. M. G. L. Gustafsson, "Surpassing the lateral resolution limit by a factor of two using structured illumination microscopy," *J. Microsc.* **198**, 82–87 (2000).
3. M. G. L. Gustafsson, L. Shao, P. M. Carlton, C. J. R. Wang, I. N. Golubovskaya, W. Z. Cande, D. A. Agard, and J. W. Sedat, "Three-dimensional resolution doubling in widefield fluorescence microscopy by structured illumination," *Biophys. J.* **94**, 4957–4970 (2008).
4. L. Shao, B. Isaac, S. Uzawa, D. A. Agard, J. W. Sedat, and M. G. L. Gustafsson, "15S: widefield light microscopy with 100-nm-scale resolution in three dimensions," *Biophys. J.* **94**, 4971–4983 (2008).
5. M. A. A. Neil, R. Juškaitis, and T. Wilson, "Real time 3D fluorescence microscopy by two beam interference illumination," *Opt. Commun.* **153**, 1–4 (1998).
6. M. A. A. Neil, A. Squire, R. Juškaitis, P. I. Bastiaens, and T. Wilson, "Wide-field optically sectioning fluorescence microscopy with laser illumination," *J. Microsc.* **197**, 1–4 (2000).
7. V. Poher, H. X. Zhang, G. T. Kennedy, C. Griffin, S. Oddos, E. Gu, D. S. Elson, M. Girkin, P. M. V. French, M. D. Dawson, and M. A. A. Neil, "Optical sectioning microscopes with no moving parts using a micro-stripe array light emitting diode," *Opt. Express* **15**, 11,196–11,206 (2007).
8. M. J. Cole, J. Siegel, S. E. D. Webb, R. Jones, K. Dowling, P. M. V. French, M. J. Lever, L. O. D. Sucharov, M. A. A. Neil, R. Juškaitis, and T. Wilson, "Whole-field optically sectioned fluorescence lifetime imaging," *Opt. Lett.* **25**, 1361–1363 (2000).
9. M. J. Cole, J. Siegel, S. E. D. Webb, R. Jones, R. Dowling, M. J. Dayel, D. Parsons-Karavassilis, P. M. V. French, M. J. Lever, L. O. D. Sucharov, M. A. A. Neil, R. Juškaitis, and T. Wilson, "Time-domain whole-field fluorescence lifetime imaging with optical sectioning," *J. Microsc.* **203**, 246–257 (2001).
10. S. E. D. Webb, Y. Gu, S. Lévêque-Fort, J. Siegel, M. J. Cole, K. Dowling, R. Jones, P. M. W. French, M. A. A. Neil, R. Juškaitis, L. O. D. Sucharov, T. Wilson, and M. J. Lever, "A wide-field time-domain fluorescence lifetime imaging microscope with optical sectioning," *Rev. Sci. Instrum.* **73**, 1898–1907 (2002).
11. L. H. Schaefer, D. Schuster, and J. Schaffer, "Structured illumination microscopy: artefact analysis and reduction utilizing a parameter optimization approach," *J. Microsc.* **216**, 165–174 (2004).
12. D. Karadaglić, "Wide-field optical sectioning microscopy," PhD Thesis, University of Oxford (2004).
13. D. Karadaglić and T. Wilson, "Image formation in structured illumination wide-field fluorescence microscopy," *Micron* **39**, 808–818 (2008).
14. B. C. Lagerholm, S. Vanni, D. L. Taylor, and F. Lanni, "Cytomechanics applications of optical sectioning microscopy," *Methods Enzymol.* **361**, 175–197 (2003).
15. F. Chasles, B. Dubertret, and A. Boccard, "Optimization and characterization of a structured illumination microscope," *Opt. Express* **15**, 16,130–16,140 (2007).
16. G. J. Brakenhoff, G. W. H. Wurpel, K. Jalink, L. Oomen, L. Brocks, and J. M. Zwier, "Characterization of sectioning fluorescence microscopy with thin uniform fluorescent layers: sectioned imaging property or SIPcharts," *J. Microsc.* **219**, 122–132 (2005).
17. A. Gennerich and D. Schild, "Anisotropic diffusion in mitral cell dendrites revealed by fluorescence correlation spectroscopy," *Biophys. J.* **83**, 510–522 (2002).
18. P. D. Nieuwkoop and J. Faber, *Normal Table of Xenopus laevis (Daudin)*, Garland Publishing, New York (1994).
19. B. J. Howell, F. W. Baumgardner, K. Bondi, and H. Rahn, "Acid-base balance in cold-blooded vertebrates as a function of body temperature," *Am. J. Physiol.* **218**, 600–606 (1970).
20. E. Linfoot and E. Wolf, "Phase distribution near focus in an aberration-free diffraction image," *Proc. Phys. Soc. London, Sect. B* **69**, 823–832 (1956).
21. J. M. Murray, "Evaluating the performance of fluorescence microscopes," *J. Microsc.* **191**, 128–134 (1998).
22. R. Heintzmann, T. M. Jovin, and C. Cremer, "Saturated patterned excitation microscopy—a concept for optical resolution improvement," *J. Opt. Soc. Am. A* **19**, 1599–1609 (2002).
23. T. Wilson, *Confocal Microscopy*, Academic Press, London (1990).
24. J. B. Pawley, *Handbook of Biological Confocal Microscopy*, Springer, Berlin (2006).
25. L. C. Kuypers, J. J. J. Dirckx, and W. F. Decraemer, "A simple method for checking the illumination profile in a laser scanning microscope and the dependence of resolution on this profile," *Scanning* **26**, 256–258 (2004).
26. J. Bewersdorf, R. Schmidt, and S. W. Hell, "Comparison of 15M and 4Pi-microscopy," *J. Microsc.* **222**, 105–117 (2006).